intermediate frequencies, $T_\theta(\omega)$ interpolates smoothly between these two limiting behaviours[12].

The behaviour seen in Fig. 2 is consistent with KTB dynamics, if we identify the crossover with T_{KTB} of an isolated bilayer. Above T_{KTB}, the conductivity is predicted to scale according to[13–15]:

$$\frac{\sigma(\omega)}{\sigma_Q} = \left(\frac{k_B T_\theta^0}{\hbar\Omega}\right) S(\omega/\Omega) \qquad (2)$$

The scaling function $S(\omega/\Omega)$ is constrained by the physics of the high- and low-frequency limits. As $\omega/\Omega \to \infty$, S must approach $i\Omega/\omega$ in order for σ to assume its superconducting form, equation (1). At low frequencies, S approaches a real constant $S_1(0)$ which characterizes the d.c. conductivity of the normal state.

By comparing the measured complex conductivity to equation (2), we can extract both the phase stiffness and correlation time at each temperature. To analyse the experimental data in terms of equation (2), we note that the phase angle of the complex conductivity, $\varphi \equiv \tan^{-1}(\sigma_2/\sigma_1)$, equals the phase angle of $S(\omega/\Omega)$. Therefore φ depends only on the single parameter Ω, and is independent of T_θ^0. With the appropriate choice of $\Omega(T)$, all the measured values of φ should collapse to a single curve when plotted as a function of the normalized frequency ω/Ω. Knowing $\Omega(T)$, T_θ^0 is obtained from a collapse of the normalized conductivity magnitude, $(\hbar\Omega/k_B T_\theta^0)|\sigma(\omega)|/\sigma_Q$, to $|S(\omega/\Omega)|$. Figure 3 shows the collapse of the data to the phase angle and magnitude of S. As anticipated, S approaches a real constant in the limit $\omega/\Omega \to 0$, and approaches $i\Omega/\omega$ as $\omega/\Omega \to \infty$.

When analysed further, the data reveal a confirmation of thermal generation of vortices in the normal state. In the KTB picture we expect that the d.c. conductivity will equal $k_B T/n_f D\Phi_0^2$, which is the 'flux-flow' conductivity of n_f free vortices with quantized flux Φ_0, and diffusivity D (ref. 16). Together with equation (2), this implies that Ω is a linear function of n_f, that is, $\Omega = \Omega_0 n_f a_{vc}/\Theta$, where a_{vc} is the area of a vortex core, $\Theta \equiv T/T_\theta^0$ is the reduced temperature, and $\Omega_0 \equiv \pi^2 S_1(0)D/a_{vc}$. Moreover, we expect that n_f will be a thermally activated function, except for T very close to T_{KTB}. The activation energy is simply $Ck_B T_\theta^0$, where C is a non-universal constant of order unity. It follows that the fluctuation frequency depends exponentially on the reciprocal of the reduced temperature, $\Omega = (\Omega_0/\Theta)\exp(-2C/\Theta)$.

The inset to Fig. 3 is a plot of $\log(\Theta\Omega)$ versus $1/\Theta$ which shows that the exponential relation is observed over nearly four orders of magnitude. This is direct evidence that vanishing of phase coherence in our samples reflects the dynamics of thermally generated vortices. From the slope and intercept of a straight-line fit we obtain $C = 2.23$ and $\Omega_0 = 1.14 \times 10^{14}\ s^{-1}$.

In Fig. 4 we present the behaviour of the bare stiffness and phase-correlation time obtained from our measurement and modelling of $\sigma(\omega)$. The main panel contrasts T_θ^0 with the dynamical stiffness $T_\theta(\omega)$ measured at 150 and 400 GHz. The inset shows τ as a function of temperature together with hatching that highlights the region where $\tau < \hbar/k_B T$.

The parameters displayed in Fig. 4 suggest that while phase correlations indeed persist above T_c, they vanish well below T^*. The loss of coherence is driven by the decrease of T_θ^0 with increasing temperature, which renders the system increasingly defenceless to the proliferation of free vortices. This decrease of T_θ^0 is consistent with a phenomenological description of a d-wave superconductor derived from a Mott insulator. In this picture, the phase stiffness of an underdoped copper oxide superconductor is undermined below T^* by the thermal generation of normal electrons very near the points in momentum space where the superconducting gap vanishes[17]. The pairing which remains in other regions of momentum space appears to contribute little to the overall phase stiffness. Near 95 K, τ falls to its minimum detectable value of $\hbar/k_B T$, which is the electron mean free time. Beyond this point, superconductivity becomes indistinguishable from the ballistic dynamics of normal electrons and the recovery of the incoherent normal state is complete. □

1. Loesser, A. G. et al. Excitation gap in the normal state of Bi₂Sr₂CaCu₂O₈₊δ. Science 273, 325–329 (1996).
2. Ding, H. et al. Spectroscopic evidence for a pseudogap in the normal state of underdoped high-T_c superconductors. Nature 382, 51–54 (1996).
3. Renner, Ch. et al. Pseudogap precursor of the superconducting gap in under- and overdoped Bi₂Sr₂CaCu₂O₈₊δ. Phys. Rev. Lett. 80, 149–152 (1998).
4. Emery, V. J. & Kivelson, S. A. Importance of phase fluctuations in superconductors with small superfluid density. Nature 374, 434–437 (1995).
5. Berezinskii, V. L. Destruction of long-range order in one-dimensional and two-dimensional systems having a continuous symmetry group I. Classical systems. Sov. Phys. JETP 32, 493–500 (1970); II. Quantum systems. Sov. Phys. JETP 34, 610–617 (1972).
6. Kosterlitz, J. M. & Thouless, D. J. Ordering, metastability and phase transitions in two-dimensional systems. J. Phys. C 6, 1181–1203 (1973).
7. Harris, J. M. et al. Anomalous superconducting state gap size versus T_c behavior in underdoped Bi₂Sr₂Ca₁₋ₓDyₓCu₂O₈₊δ. Phys. Rev. B 54, 15665–15668 (1996).
8. Doniach, S. & Inui, M. Long-range Coulomb interactions and the onset of superconductivity in the high-T_c materials. Phys. Rev. B 41, 6668–6678 (1990).
9. Nuss, M. C. & Orenstein, J. in Millimeter and Submillimeter Spectroscopy of Solids (ed. Grüner, G.) 7–50 (Topics in Applied Physics Vol. 74, Springer, New York, 1998).
10. Eckstein, J. N. & Bozovic, I. High-temperature superconducting multilayers and heterostructures grown by atomic layer-by-layer molecular beam epitaxy. Annu. Rev. Mater. Sci. 25, 679–709 (1995).
11. Kosterlitz, J. M. & Nelson, D. R. Universal jump in the superfluid density of two-dimensional superfluids. Phys. Rev. Lett. 39, 1201–1205 (1977).
12. Ambegaokar, V., Halperin, B. I., Nelson, D. R. & Siggia, E. D. Dynamics of superfluid films. Phys. Rev. B 20, 1806–1826 (1980).
13. Halperin, B. I. & Nelson, D. R. Resistive transition in superconducting films. J. Low Temp. Phys. 36, 599–616 (1979).
14. Minnhagen, P. The two-dimensional Coulomb gas, vortex unbinding, and superfluid-superconducting films. Rev. Mod. Phys. 59, 1001–1066 (1987).
15. Jonsson, A. & Minnhagen, P. Characteristics of two-dimensional vortex dynamics from XY-type models with Ginzburg–Landau dynamics. Phys. Rev. B 55, 9035–9046 (1997).
16. Bardeen, J. & Stephen, M. J. Theory of the motion of vortices in superconductors. Phys. Rev. A 140, 1197–1207 (1965).
17. Lee, P. A. & Wen, X. G. Unusual superconducting state of underdoped cuprates. Phys. Rev. Lett. 78, 4111–4114 (1997).

Aerosol-assisted self-assembly of mesostructured spherical nanoparticles

Yunfeng Lu*, Hongyou Fan*, Aaron Stump*, Timothy L. Ward*, Thomas Rieker* & C. Jeffrey Brinker*†

* University of New Mexico/NSF Center for Micro-Engineered Materials, The Advanced Materials Laboratory, 1001 University Boulevard SE, Albuquerque, New Mexico 87106, USA
† Sandia National Laboratories, Direct Fabrication Department, 1831, Albuquerque, New Mexico 87185, USA

Particles possessing nanometre-scale pores of well-defined size and connectivity are of interest for catalysis, chromatography and controlled release of drugs, and as fillers with low dielectric constant, pigments and hosts for optically active compounds[1,2]. Silica containing ordered mesopores (of nanometre-scale width) can be prepared by templating of surfactant[3,4] and block copolymer[5] liquid-crystalline mesophases, and interfacial phenomena have been used to control the macroscopic form of these materials, providing mesoporous particles[1,6], fibres[7,8] and films[9,10]. A variety of spherical or nearly spherical particles has been reported[1,6,7,11–13], but the degree of ordering and the range of the porous mesostructures have been limited. Here we report a rapid, aerosol-based[14–16] process for synthesizing solid, well-ordered spherical particles with stable pore mesostructures of hexagonal and cubic topology, as well as layered (vesicular) structures. Our method relies on evaporation-induced interfacial self-assembly[17] confined to spherical aerosol droplets. This simple, generalizable process can be modified for the formation of ordered meso-structured thin films.

Schacht et al.[6] first demonstrated that mesoscopically ordered hollow spheres could be prepared by interfacial reactions conducted in oil/water emulsions with varying extents of imposed shear. Huo et al.[1] extended this general emulsion-based approach to prepare spheres with diameters of 0.1–2.0 mm. Tanev and Pinnavaia[12] condensed silica in the interlayer regions of multilamellar vesicles to form roughly spherical particles with stable lamellar mesostructures. Bruinsma et al.[7] used spray drying to prepare hollow spherical particles or collapsed, irregular particles. These various pathways to the preparation of nominally spherical mesostructured particles have so far resulted in irregular shapes and/or particles with non-uniform or ill-defined mesostructures.

Our process starts with a homogeneous solution of soluble silica plus surfactant prepared in an ethanol/water solvent with initial surfactant concentration c_0 much less than the critical micelle concentration c.m.c. Using the apparatus depicted in Fig. 1, we generate an aerosol dispersion within a tubular reactor. In a continuous, ~6-second process, the aerosol particles are dried, heated and collected. As recently demonstrated for thin-film formation[17], preferential alcohol evaporation[18] during drying enriches the particles in surfactant, water and silica, inducing micelle formation and successive co-assembly of silica–surfactant micellar species into liquid-crystalline mesophases. The resulting particles are commonly solid, with highly ordered hexagonal, cubic or vesicular mesostructures (Fig. 2). Through introduction of metal complexes or organic dyes/precursors into the starting solution, we can use the same process to prepare ordered nanocomposite particles (Fig. 3).

Figure 2 shows representative transmission electron microscope (TEM) images of calcined silica particles prepared using CTAB, Brij-58, Brij-56 or P123 templates (see Methods for details of templates). Figure 3 shows TEM images of various metal–, organic– and polymer–silica nanocomposite particles. CTAB produces particles exhibiting a highly ordered hexagonal mesophase over the concentration range $c_0 = 0.06$–0.16 M (Figs 2a and 3a). Many of the particles adopted a polyhedral shape that is hexagonal in cross-section, a macroscopic manifestation of the local packing geometry[19]. Use of the non-ionic surfactants (Brij-56/58) commonly resulted in vesicular mesostructures, but cubic and hexagonal mesostructures were also attainable (Figs 2b and 3b). Distinct from related bulk and thin-film lamellar structures that collapse on calcination[20], the three-dimensional connectivity of the nested spherical shells comprising the vesicular mesophase mechanically stabilizes the structure against collapse during surfactant removal. Under processing conditions where the outer silica shells solidify before the drying shrinkage is complete, uniform dimpling of the shell surface results (Fig. 3c), in order to preserve the solidified shell surface area. This may be contrasted with the shrinkage-induced formation of toroidal or raisin-like collapsed morphologies commonly observed for spray-dried powders[7].

Figure 4 shows small-angle X-ray scattering (SAXS) data for calcined mesostructured silica particles prepared with CTAB, Brij-56 and P123 surfactants, along with the corresponding N_2 sorption isotherms ('as-prepared' particles had no internal surface area accessible to N_2 owing to retention of the surfactant templates). The main peak is indexed as the [100]-reflection of the hexagonal (CTAB) and vesicular mesophases. SAXS and N_2 sorption show the expected increase in d-spacing and pore size with increasing surfactant volume/molecular mass (CTAB < Brij-56 < P123).

The robustness of our evaporation-induced interfacial self-assembly (EISA) process, combined with the short residence time of the particles in the furnace, enable us to prepare a variety of mesostructured organic/silica, metal/silica and even enzyme/silica composite particles while retaining the respective structure, function and bio-activity of the guest species (A.S. and R. Bhatia, unpublished results). Furthermore, through addition of organic monomers and thermal initiators to the parent solution, we can co-organize and polymerize mesostructured silica–polymer nanocomposite particles, as recently demonstrated for coatings[21]. The mesostructures shown in Fig. 3 illustrate the diversity of nanocomposite
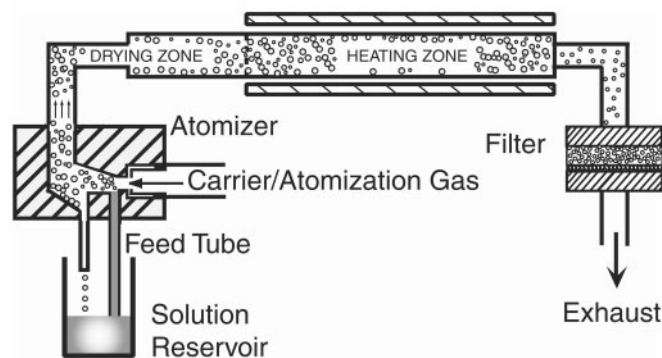

Figure 1 Diagram of aerosol reactor. Silica/surfactant aerosols were generated using a commercial atomizer (Model 3076, TSI, Inc., St Paul, MN) operated with nitrogen as a carrier/atomization gas. This atomizer produces aerosol droplets with a size distribution characterized by a geometric standard deviation of 2 (95% of the particles have diameters between 0.25 and 4 times the mean diameter). The pressure drop at the pinhole was 2.4 atm. Particles were collected on a Teflon filter, TEM grid, or silicon substrate maintained at 80 °C. For film experiments the furnace was not operated. For one experiment, HCl vapour was introduced into the reactor through a coaxial tube positioned at the centre of the heating zone.
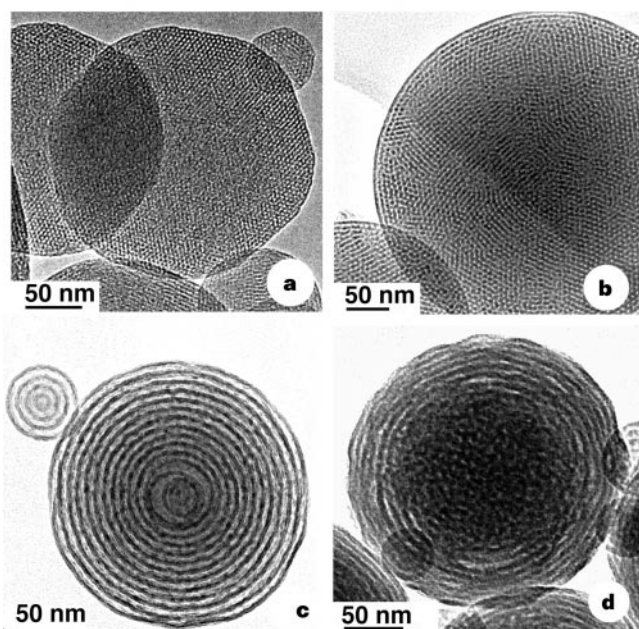

Figure 2 Representative TEM micrographs of mesostructured silica particles. **a**, Faceted, calcined particles with a hexagonal mesophase ($d_{100} = 32.5$ Å). The sol was prepared using 5 wt% CTAB as the surfactant template and molar ratio TEOS:EtOH:water:HCl:CTAB = 1:22:5:0:0.004:0.15. **b**, Calcined particles showing cubic mesostructure. The sol was prepared using 4.2 wt% Brij-58 as the surfactant template and molar ratio TEOS:EtOH:water:HCl:Brij-58 = 1:0:67:0.004:0.046. **c**, Calcined particles showing a vesicular mesophase ($d_{100} = 92$ Å). The sol was prepared using 5% P123 as the triblock copolymer template, and molar ratio TEOS:EtOH:water:HCl:P123 = 1:22:5:0.004:0.0096. **d**, Uncalcined silica particles showing 'growth' of ordered vesicular domains from the liquid–vapour interface. The particle interior has a disordered, worm-like mesostructure. The sol was prepared using 2.5% Brij-56 as the surfactant template, and molar ratio TEOS:EtOH:water:HCl:Brij-56 = 1:13:67:0.004:0.04. All calcination treatments were performed at 425 °C for 3 h in air (heating rate, 1 °C min⁻¹).

constructions and materials combinations attainable by our method.

Evaporation during aerosol processing creates within each droplet a radial gradient in surfactant concentration that steepens with time[22] and maintains a maximum concentration at the droplet surface. Starting with an initially homogeneous solution (with c_0 less than the c.m.c.), the surfactant critical micelle concentration is exceeded first at the surface of the droplet, and, as evaporation proceeds, is progressively exceeded throughout the droplet. This surfactant enrichment induces silica–surfactant self-assembly into
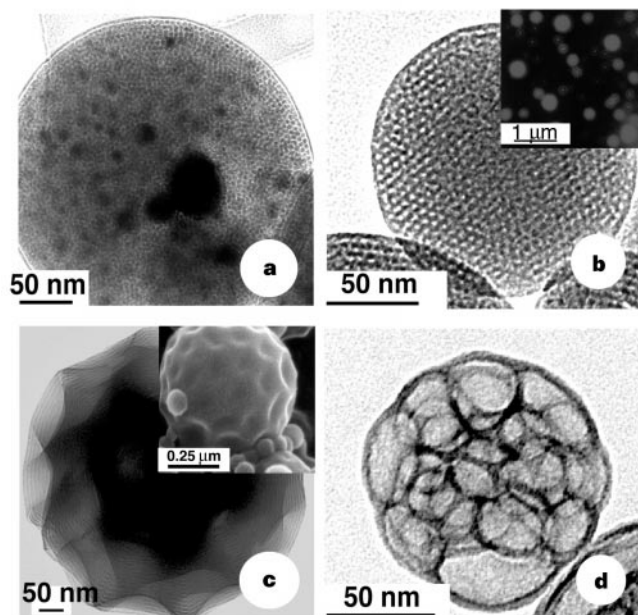
micelles and further organization into liquid-crystalline meso-phases. The radial concentration gradient and the presence of the liquid–vapour interface (which serves as a nucleating surface[9,17,23]) causes ordered silica–surfactant liquid-crystalline domains to grow radially inward (Fig. 2d) rather than outwards from a seed[24]. Crucial for the formation of solid, completely ordered particles is main-tenance of a liquid, or liquid-crystalline, state throughout the course of the EISA process. Premature solidification would result in the formation of hollow particles[7] and inhibit orderly self-assembly that must proceed with continual restructuring of the evolving silica–surfactant mesophase in order to accommodate drying shrinkage. Evidence for such a semi-solid state is the formation of continuous, uniform films on the collection surface when the furnace is main-tained at low temperature ($<150\,°C$). As shown in Fig. 5, film formation occurs via droplet coalescence. The resulting films are highly ordered, which is important for applications such as mem-branes, and can span holes hundreds of times greater in diameter than the film thickness.

We note that the curvature of the particle surface profoundly influences mesostructure development. This is evident in the comparison of CTAB-templated particles (Fig. 2a) with the corre-sponding mesostructured films formed on flat substrates by EISA during dip-coating[17]. Unlike films—which have flat liquid–vapour interfaces and show a progressive change in mesostructure (disordered → hexagonal → cubic → lamellar) with increasing sur-factant concentration[17]—particles prepared with comparable CTAB

Figure 3 TEM micrographs of a variety of nanocomposite particles. **a**, Silica/gold nanocomposite particle with an ordered hexagonal mesostructure. Colloidal gold (particle size 1–3 nm) was prepared in inverse micelles according to the method of Brust *et al.*[28], using 1-dodecanethiol as a stabilizing agent. The gold colloids were added to a silica/5 wt% CTAB sol, prepared with molar ratio TEOS:EtOH:water:HCl:CTAB = 1:0:67:0.004:0.15. During aerosol processing, hydrophobic gold colloids partition into the hydrophobic micellar interiors and are subsequently incorporated in the hexagonal mesophase. TEM and X-ray diffraction indicate $d_{100} = ~60\,Å$, (compared to 32.5 Å; Fig. 2a), consistent with incorporation of the gold colloids in the hexagonal silica mesophase. **b**, Fluo-rescent silica/rhodamine B nanocomposite particles exhibiting a hexagonal mesophase. The sol was prepared by adding 0.8 wt% rhodamine B to a silica/4.2 wt% Brij-56 sol prepared with molar ratio TEOS:EtOH:water:HCl:Brij-56 = 1:13:67:0.004:0.068. Inset, optical photomicrograph of the fluorescence emission imaged through a rhodamine B filter, confirming retention of the dye structure. Samples were exhaustively washed before optical microscopy. **c**, Silica/polymer nanocomposite particle showing puckered vesicular mesostructure (inset, SEM image showing uniform periodic dimpling). The sol was prepared by adding poly(propylene glycol dimethacrylate) (PPO, molecular mass 660) and thermal initiator, 1,1'-azobis (1-cyclohexanecarbonitrile) (ACHN) to a silica/5 wt% P123 sol prepared with molar ratio TEOS:ethanol:water:HCl:P123:PPO:ACHN = 1:22:5:0.004:0.0096:0.025:0.009. During aerosol processing, the oligomer and initiator are incorporated into the hydrophobic portion of the template bilayers[21] resulting in thermally initiated polymerization of PPO. **d**, Silica/polymer nano-composite particle showing reticulated foam structure. The sol was prepared as in **c** but with molar ratio TEOS:ethanol:water:HCl:P123:PPO:ACHN = 1:13:67:0.004:0.0096:0.025:0.009. The greater water concentration compared to **c** resulted in micelle formation (in the starting sol) and incorporation of PPO and ACHN into the micellar interiors. Subsequent micelle coalescence combined with thermally initiated polymerization during aerosol processing resulted in the reticulated nanostructure.
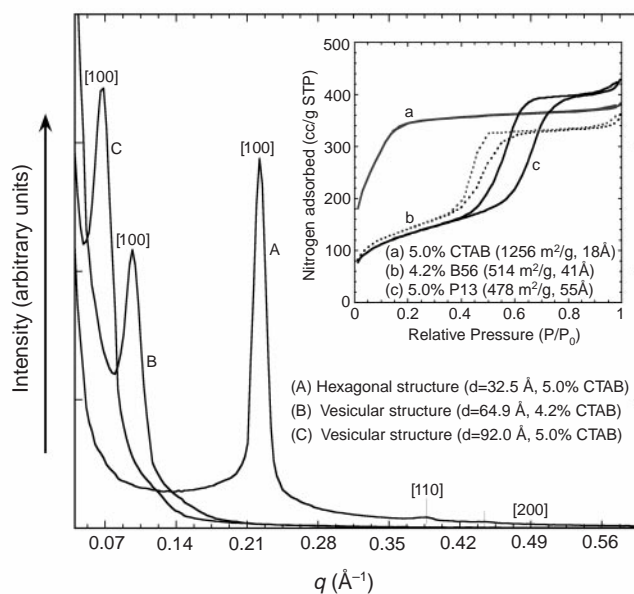

Figure 4 Small-angle X-ray scattering (SAXS) curves for silica particles with hexagonal (trace A) or vesicular (B and C) mesophases. Samples A and C were prepared as in Fig. 2a and c, respectively. Sample B was obtained for calcined particles showing a vesicular mesostructure ($d_{100} = 65$ Å). The sol was prepared using 4.2 wt% Brij-56 as the surfactant template, and molar ratio TEOS:EtOH:water:HCl: Brij-56 = 1:13:67:0.004:0.068. Inset, Corresponding N_2 adsorption--desorption isotherms, BET surface areas, and pore diameters. (We note that the calculated pore diameter of sample A is slightly less than 2.0 nm, the lower limit of mesoporosity according to the IUPAC definition. Thus the validity of the BET expression is questionable). SAXS experiments were performed at the University of New Mexico/Sandia National Laboratories SAXS facility[29]. Samples (~0.5 mm thick) were prepared by sprinkling powder on adhesive cellophane tape used as a 1.5-cm-diameter window. SAXS data were collected (30 min per run) using the 5-m pinhole instrument in short geometry ($0.3 < q < 7\,nm^{-1}$, where q is defined as $(4\pi/\lambda)\sin(2\theta/2)$, and 2θ is the scattering angle). SAXS data are uncorrected for background. Hydraulic pore diameters were calculated from the pore volume and BET surface area.
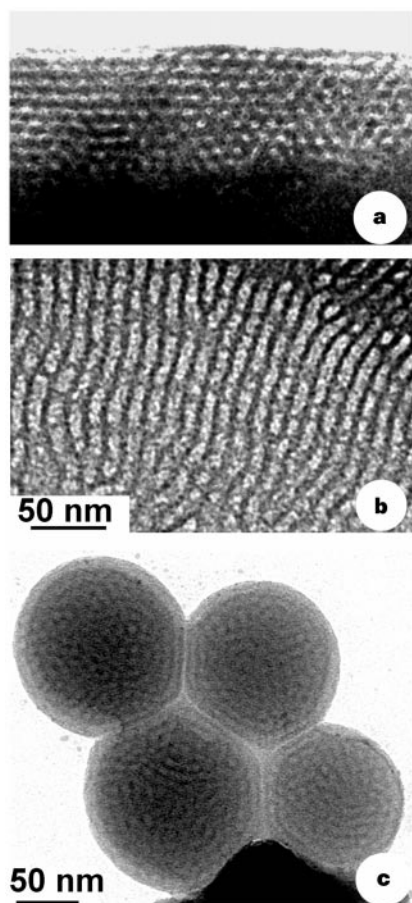
Figure 5 TEM images of mesostructured films formed by an aerosol-assisted thin film deposition route. A 5 wt% P123 sol (identical to that in Fig. 2c) was used. **a**, Cross-sectional TEM image of hexagonal mesostructured film deposited on silicon substrate. **b**, Plan-view image of hexagonal mesostructured film deposited on holey carbon grid. **c**, TEM image of corresponding aerosol droplets during coalescence on a holey carbon grid. For **a** and **b**, film samples were prepared using the apparatus shown in Fig. 1, but without operation of the furnace and with replacement of the filter with a silicon substrate (**a**) or holey carbon grid (**b**). The partially coalesced droplets (**c**) were prepared as in **b** but with introduction of HCl vapour to promote silica condensation and thereby 'freeze-in' the evolving mesostructure before complete coalescence. From **c** we conclude that film formation is possible by avoidance of particle solidification. The semi-solid nature of the particles (along with their low surface tensions) enables film formation over holes much greater in diameter than the film thickness.

concentrations show only disordered or hexagonal mesophases. We conclude that, because the liquid–vapour interface serves as a nucleating surface for liquid-crystal growth, the high curvature imposed by this interface alters the generally observed relationship between the surfactant packing parameter and the resulting mesostructure[25]. Although CTAB commonly forms lamellar mesophases in bulk and thin-film samples[3,20,26], it appears that this molecule cannot pack into a cone truncated by surfaces of high and opposite curvature, as needed to direct the vesicular mesostructure. Only surfactants containing ethylene oxide (EO) blocks consistently gave vesicular mesophases. □

Methods

Precursor solutions were synthesized by the addition of cationic surfactant (CTAB; $CH_3(CH_2)_{15}N^+(CH_3)_3Br^-$), non-ionic surfactant (Brij-56; $CH_3(CH_2)_{15}-(OCH_2CH_2)_{10}-OH$: Brij-58; $CH_3(CH_2)_{15}-(OCH_2CH_2)_{20}-OH$) or triblock copolymers (Pluronic-P123; $(EO)_{20}$(propylene oxide, $PO)_{70}(EO)_{20}$) to an acidic silica sol (A2**). The acid concentration employed in the A2**

synthesis procedure was chosen to minimize the siloxane condensation rate[27], thereby promoting facile silica–surfactant self-assembly during aerosol processing. In a typical preparation, TEOS [$Si(OCH_2CH_3)_4$], ethanol, water and dilute HCl (mole ratios: 1:3.8:1:5 × 10^{-5}) were refluxed at 60 °C for 90 min. The sol was diluted with ethanol (1:2) followed by addition of water and dilute HCl. Surfactants were added in the amounts needed to achieve initial surfactant concentrations c_0 ranging from 0.004 to 0.23 M. The final reactant mole ratios (TEOS:EtOH:H_2O:HCl:surfactant) were 1:(0–22):(5–67):0.004:(0.006–0.23). Sols used to prepare various nanocomposite particles were synthesized by addition of organosilates, organic dyes, polymers, metal colloids, or commercial catalysts directly to the precursor solutions.

Spherical mesostructured particles were prepared using an aerosol reactor (Fig. 1) operated at a volumetric flow rate of 2.6 l STP min^{-1}. Under these conditions, the flow is laminar (Reynolds number at 400 °C, 75) and the entrained aerosol particles experience ~3 s of drying at nominally room temperature followed by ~3 s of heating at 400 °C and finally collection on a filter maintained at 80 °C. The collected particles were characterized by TEM, SAXS, and N_2 sorption before and after calcination at 425 °C in air or N_2 (heating rate, 1 °C min^{-1}) to remove the surfactant templates.

1. Huo, Q., Feng, J., Schuth, F. & Stucky, G. D. Preparation of hard mesoporous silica spheres. *Chem. Mater.* **9,** 14–17 (1997).
2. Ozin, G. Nanochemistry: synthesis in diminishing dimensions. *Adv. Mater.* **4,** 612–649 (1992).
3. Kresge, C., Leonowicz, M., Roth, W., Vartuli, C. & Beck, J. Ordered mesoporous molecular sieves synthesized by a liquid-crystal template mechanism. *Nature* **359,** 710–712 (1992).
4. Yang, H., Coombs, N. & Ozin, G. Mesoporous silica with micrometer-scale designs. *Adv. Mater.* **9,** 811–814 (1997).
5. Zhao, D. *et al.* Triblock copolymer syntheses of mesoporous silica with periodic 50 and 300 Angstrom pores. *Science* **279,** 548–552 (1998).
6. Schacht, S., Huo, Q., Voigt-Martin, I. G., Stucky, G. D. & Schuth, F. Oil-water interface templating of mesoporous macroscale structures. *Science* **273,** 768–771 (1996).
7. Bruinsma, P. J., Kim, A. Y., Liu, J. & Baskaran, S. Mesoporous silica synthesized by solvent evaporation: Spun fibers and spray-dried hollow spheres. *Chem. Mater.* **9,** 2507–2512 (1997).
8. Yang, P., Zhao, D., Chmelka, B. F. & Stucky, G. D. Triblock-copolymer-directed syntheses of large-pore mesoporous silica fibers. *Chem. Mater.* **10,** 2033–2036 (1998).
9. Yang, H., Coombs, N., Sokolov, I. & Ozin, G. Free-standing and oriented mesoporous silica films grown at the air-water interface. *Nature* **381,** 589–592 (1996).
10. Aksay, I. *et al.* Biomimetic pathways for assembling inorganic thin films. *Science* **273,** 892–898 (1996).
11. Grun, M., Lauer, I. & Unger, K. K. The synthesis of micrometer- and submicrometer-size spheres of ordered mesoporous oxide MCM-41. *Adv. Mater.* **9,** 254–257 (1997).
12. Tanev, P. & Pinnavaia, T. Biomimetic templating of porous lamellar silicas by vesicular surfactant assemblies. *Science* **271,** 1267–1269 (1996).
13. Yang, H., Vovk, G., Coombs, N., Sokolov, I. & Ozin, G. A. Synthesis of mesoporous silica spheres under quiescent aqueous acidic conditions. *J. Mater. Chem.* **8,** 743–750 (1998).
14. Messing, G. L., Zhang, S.-C. & Jayanthi, G. V. Ceramic powder synthesis by spray pyrolysis. *J. Am. Ceram. Soc.* **76,** 2707–2726 (1993).
15. Gurav, A., Kodas, T. T., Pluym, T. & Xiong, Y. Aerosol processing of materials. *Aerosol Sci. Technol.* **19,** 411–452 (1993).
16. Pratsinis, S. E. & Mastrangelo, S. V. R. Material synthesis in aerosol reactors. *Chem. Eng. Prog.* **85,** 62–66 (1989).
17. Lu, Y. *et al.* Continuous formation of supported cubic and hexagonal mesoporous films by sol-gel dip-coating. *Nature* **389,** 364–368 (1997).
18. Nishida, F. *et al. In situ* fluorescence probing of the chemical changes during sol-gel thin film formation. *J. Am. Ceram. Soc.* **78,** 1640–1648 (1995).
19. Alfredsson, V. *et al.* Cubosome description of the inorganic mesoporous structure MCM-48. *Chem. Mater.* **9,** 2066–2070 (1997).
20. Ogawa, M. Formation of novel oriented transparent films of layered silica-surfactant nanocomposites. *J. Am. Chem. Soc.* **116,** 7941–7942 (1994).
21. Sellinger, A. *et al.* Continuous self-assembly of organic-inorganic nanocomposite coatings that mimic nacre. *Nature* **394,** 256–260 (1998).
22. Jayanthi, G. V., Zhang, S. C. & Messing, G. L. Modeling of solid particle formation during solution aerosol thermolysis. *Aerosol Sci. Technol.* **19,** 478–490 (1993).
23. Yang, H., Coombs, N., Dag, O., Sokolov, I. & Ozin, G. Free-standing mesoporous silica films; morphogenesis of channel and surface patterns. *J. Mater. Chem.* **7,** 1755–1761 (1997).
24. Yang, H., Coombs, N. & Ozin, G. A. Morphogenesis of shapes and surface patterns in mesoporous silica. *Nature* **386,** 692–695 (1997).
25. Israelachvili, J. *Intramolecular and Surface Forces* (Academic, San Diego, 1992).
26. Bull, L. M. *et al.* in *Zeolites and Related Microporous Materials: State of the Art 1994* (eds Bull, L. M. *et al.*) 429–434 (Elsevier Science, Amsterdam, 1994).
27. Brinker, C., Sehgal, R., Raman, N., Schunk, P. & Headley, T. Polymer approach to supported silica membranes. *Sol-Gel Sci. Technol.* **2,** 469–476 (1994).
28. Brust, M., Walker, M., Bethell, D., Schiffrin, D. J. & Whyman, R. Synthesis of thiol-derivatized gold nanoparticles in a 2-phase liquid-liquid system. *J. Chem. Soc. Chem. Commun.* **7,** 801–802 (1994).
29. Reiker, T. P. & Hubbard, P. F. The University of New Mexico/Sandia National Laboratories small-angle x-ray scattering laboratory. *Rev. Sci. Instrum.* (submitted).